5306 *Chem. Mater.* **2010,** *22,* 5306–5313
DOI:10.1021/cm101532x

CHEMISTRY OF MATERIALS
Article

Graphene-Wrapped Fe_3O_4 Anode Material with Improved Reversible Capacity and Cyclic Stability for Lithium Ion Batteries

Guangmin Zhou,[†] Da-Wei Wang,[‡] Feng Li,*[,†] Lili Zhang,[†] Na Li,[†] Zhong-Shuai Wu,[†] Lei Wen,[†] Gao Qing (Max) Lu,[‡] and Hui-Ming Cheng*[,†]

[†]*Shenyang National Laboratory for Materials Science, Institute of Metal Research, Chinese Academy of Sciences, 72 Wenhua Road, Shenyang 110016, P. R. China, and* [‡]*ARC Centre of Excellence for Functional Nanomaterials, AIBN, The University of Queensland, St Lucia, Brisbane 4072, Australia*

Received June 1, 2010. Revised Manuscript Received August 12, 2010

A well-organized flexible interleaved composite of graphene nanosheets (GNSs) decorated with Fe_3O_4 particles was synthesized through in situ reduction of iron hydroxide between GNSs. The GNS/Fe_3O_4 composite shows a reversible specific capacity approaching 1026 mA h g^{-1} after 30 cycles at 35 mA g^{-1} and 580 mAh g^{-1} after 100 cycles at 700 mA g^{-1}as well as improved cyclic stability and excellent rate capability. The multifunctional features of the GNS/Fe_3O_4 composite are considered as follows: (i) GNSs play a "flexible confinement" function to enwrap Fe_3O_4 particles, which can compensate for the volume change of Fe_3O_4 and prevent the detachment and agglomeration of pulverized Fe_3O_4, thus extending the cycling life of the electrode; (ii) GNSs provide a large contact surface for individual dispersion of well-adhered Fe_3O_4 particles and act as an excellent conductive agent to provide a highway for electron transport, improving the accessible capacity; (iii) Fe_3O_4 particles separate GNSs and prevent their restacking thus improving the adsorption and immersion of electrolyte on the surface of electroactive material; and (iv) the porosity formed by lateral GNSs and Fe_3O_4 particles facilitates ion transportation. As a result, this unique laterally confined GNS/Fe_3O_4 composite can dramatically improve the cycling stability and the rate capability of Fe_3O_4 as an anode material for lithium ion batteries.

1. Introduction

Lithium ion batteries (LIBs) can store and supply electricity over a long period, and their utilization has been increasing, from civil to military applications.[1−3] Electrode materials, i.e., anode and cathode materials, play dominant roles in the performance of LIBs. Significant achievements have been gained in the research of anode materials with superior capacity, such as Si,[4,5] Sn[6,7] and transition metal oxides.[8−16] Among these potential anode materials, Fe_3O_4 shows high capacity, low cost, eco-friendliness, and natural abundance, thus has attracted considerable attention.[17−21] For instance, carbon-coated Fe_3O_4 nanospindles,[17] carbon-decorated single-crystalline Fe_3O_4 nanowires,[18] Fe_3O_4-based Cu nanoarchitecture,[19] magnetite/carbon core−shell nanorods,[20] and iron oxide-based nanotube arrays[21] have been used to improve the electrochemical performance of iron oxides. However, these high-capacity materials are still plagued with a problem of rapid capacity fading because of pulverization during cycling, which leads to the breakdown

*Corresponding author. E-mail: cheng@imr.ac.cn (H.-M.C); fli@imr.ac.cn (F.L.).

(1) Tarascon, J. M.; Armand, M. *Nature* **2001**, *414*, 359–367.
(2) Bruce, P. G.; Scrosati, B.; Tarascon, J. M. *Angew. Chem., Int. Ed.* **2008**, *47*, 2930–2946.
(3) Kim, M. G.; Cho, J. *Adv. Funct. Mater.* **2009**, *19*, 1497–1514.
(4) Gao, B.; Sinha, S.; Fleming, L.; Zhou, O. *Adv. Mater.* **2001**, *13*, 816–819.
(5) Chan, C. K.; Peng, H. L.; Liu, G.; McIlwrath, K.; Zhang, X. F.; Huggins, R. A.; Cui, Y. *Nat. Nanotech.* **2008**, *3*, 31–35.
(6) Lee, K. T.; Jung, Y. S.; Oh, S. M. *J. Am. Chem. Soc.* **2003**, *125*, 5652–5653.
(7) Derrien, G.; Hassoun, J.; Panero, S.; Scrosati, B. *Adv. Mater.* **2007**, *19*, 2336–2340.
(8) Poizot, P.; Laruelle, S.; Grugeon, S.; Dupont, L.; Tarascon, J. M. *Nature* **2000**, *407*, 496–499.
(9) Nam, K. T.; Kim, D. W.; Yoo, P. J.; Chiang, C. Y.; Meethong, N.; Hammond, P. T.; Chiang, Y. M.; Belcher, A. M. *Science* **2006**, *312*, 885–888.
(10) Li, Y. G.; Tan, B.; Wu, Y. Y. *Nano Lett.* **2008**, *8*, 265–270.
(11) Reddy, M. V.; Yu, T.; Sow, C. H.; Shen, Z. X.; Lim, C. T.; Rao, G. V. S.; Chowdari, B. V. R. *Adv. Funct. Mater.* **2007**, *17*, 2792–2799.
(12) Chen, J.; Xu, L. N.; Li, W. Y.; Gou, X. L. *Adv. Mater.* **2005**, *17*, 582–586.
(13) Cui, Z. M.; Hang, L. Y.; Song, W. G.; Guo, Y. G. *Chem. Mater.* **2009**, *21*, 1162–1166.
(14) Zhi, L. J.; Hu, Y. S.; El Hamaoui, B.; Wang, X.; Lieberwirth, I.; Kolb, U.; Maier, J.; Mullen, K. *Adv. Mater.* **2008**, *20*, 1727–1731.
(15) Wang, Y.; Su, F. B.; Lee, J. Y.; Zhao, X. S. *Chem. Mater.* **2006**, *18*, 1347–1353.
(16) Lou, X. W.; Wang, Y.; Yuan, C. L.; Lee, J. Y.; Archer, L. A. *Adv. Mater.* **2006**, *18*, 2325–2329.
(17) Zhang, W. M.; Wu, X. L.; Hu, J. S.; Guo, Y. G.; Wan, L. J. *Adv. Funct. Mater.* **2008**, *18*, 3941–3946.
(18) Muraliganth, T.; Murugan, A. V.; Manthiram, A. *Chem. Commun.* **2009**, 7360–7362.
(19) Taberna, L.; Mitra, S.; Poizot, P.; Simon, P.; Tarascon, J. M. *Nat. Mater.* **2006**, *5*, 567–573.
(20) Liu, H.; Wang, G. X.; Wang, J. Z.; Wexler, D. *Electrochem. Commun.* **2008**, *10*, 1879–1882.
(21) Liu, J. P.; Li, Y. Y.; Fan, H. J.; Zhu, Z. H.; Jiang, J.; Ding, R. M.; Hu, Y. Y.; Huang, X. T. *Chem. Mater.* **2010**, *22*, 212–217.

Published on Web 08/26/2010

of electrical connection of anode materials from current collectors.

Strategies have been proposed to mitigate the pulverization and further enhance the structural stability of electrode materials, such as nanostructuring, designing unique configurations, controlling pore structures, and a combination of micro/nanostructures, which are expected to conquer the challenge with good cyclic performance as well as to maintain high specific capacity.[22] The concepts of inner-pore or internanotube confinement are utilized to disperse metal or metal oxide particles to ordered mesoporous carbon[23,24] or carbon nanotubes[25,26] to release the volume expansion, while improving the cycling stability. However, the large specific surface area of mesoporous carbon raises the risk of secondary reactions for electrolyte decomposition[17] and the stiff carbon framework is not good for buffering the huge volume expansion. With respect to the void space inside a nanotube, the restricted inner surface area is insufficient for active materials to be well adhered and homogeneously distributed. A carbon coating is widely used for preventing the exfoliation of the inner active material as well as improving the electrical conductivity of electrode materials, such as carbon decorated Si,[27,28] SnO_2,[29,30] and iron oxides.[17,18,31,32] Because the carbon coating tightly wraps the surface of the active materials, it somehow cannot effectively release the large strain caused by volume expansion and also increases the resistance for lithium ion to reach the core of active materials. Recently, a new type of nanoarchitecture, a hollow structure together with carbon coating, was proposed and it manifests improved cycling performance and rate capability.[33,34] To circumvent the challenges faced by inner-pore filling or exterior coating, a flexible confining structure is expected to provide enough buffer space for improving the cycling stability of anode materials by reducing the pulverization.

Scheme 1. Schematic of a Flexible Interleaved Structure Consisting of GNSs and Fe_3O_4 Particles

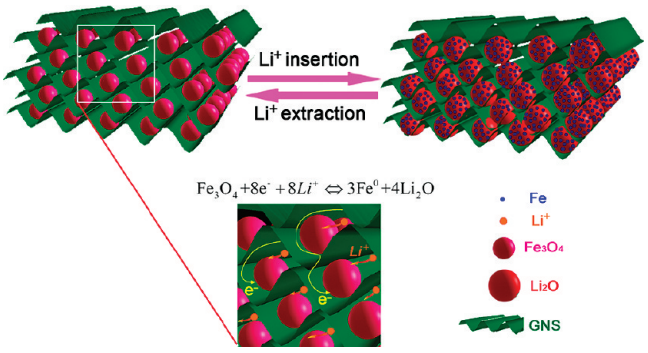

Graphene nanosheets (GNSs) possess an open porous system.[35] More importantly, the porous texture of GNSs causes the material to be flexible due to the lack of rigid connections between adjacent nanosheets. This flexible porous system could be used as a confining structure with substantial buffering capability to reduce electrode pulverization. Additionally, GNSs also have excellent electrical conductivity.[36−38] Inspired by these features, graphene and graphene-based materials have been recently explored in LIBs.[39−47] However, the aggregation of GNSs makes it difficult to demonstrate their superior properties. Therefore, we take the advantages of the characteristics of GNSs to construct a unique flexible interleaved structure with layer-by-layer of GNS and oxide anode materials, uniting the two building blocks for reducing the pulverization of these materials and enhancing their cycling stability, as well as inhibiting the degree of restacking of GNSs. The interleaved network of GNSs produce pathways for electron transport (Scheme 1), and can obviously improve the electrical conductivity of the electrode. It is expected that such a flexible confining structure can be used to fabricate other composite anode materials with metals or metal oxides. Herein, we report an easy approach for obtaining a well-organized flexible interleaved composite of GNSs decorated

(22) Liu, C.; Li, F.; Ma, L.-P.; Cheng, H.-M. *Adv. Mater.* **2010**, *22*, E28–E62.
(23) Fan, J.; Wang, T.; Yu, C. Z.; Tu, B.; Jiang, Z. Y.; Zhao, D. Y. *Adv. Mater.* **2004**, *16*, 1432–1436.
(24) Grigoriants, I.; Sominski, L.; Li, H. L.; Ifargan, I.; Aurbach, D.; Gedanken, A. *Chem. Commun.* **2005**, 921–923.
(25) Kumar, T. P.; Ramesh, R.; Lin, Y. Y.; Fey, G. T. K. *Electrochem. Commun.* **2004**, *6*, 520–525.
(26) An, G. M.; Na, N.; Zhang, X. R.; Miao, Z. J.; Miao, S. D.; Ding, K. L.; Liu, Z. M. *Nanotechnology* **2007**, *18*, 435707.
(27) Hu, Y. S.; Demir-Cakan, R.; Titirici, M. M.; Muller, J. O.; Schlogl, R.; Antonietti, M.; Maier, J. *Angew. Chem., Int. Ed.* **2008**, *47*, 1645–1649.
(28) Yoshio, M.; Wang, H. Y.; Fukuda, K.; Umeno, T.; Dimov, N.; Ogumi, Z. *J. Electrochem. Soc.* **2002**, *149*, A1598–A1603.
(29) Lou, X. W.; Chen, J. S.; Chen, P.; Archer, L. A. *Chem. Mater.* **2009**, *21*, 2868–2874.
(30) Moon, T.; Kim, C.; Hwang, S. T.; Park, B. *Electrochem. Solid State Lett.* **2006**, *9*, A408–A411.
(31) Piao, Y. Z.; Kim, H. S.; Sung, Y. E.; Hyeon, T. *Chem. Commun.* **2010**, *46*, 118–120.
(32) Wang, L.; Yu, Y.; Chen, P. C.; Zhang, D. W.; Chen, C. H. *J. Power Sources* **2008**, *183*, 717–723.
(33) Lou, X. W.; Deng, D.; Lee, J. Y.; Archer, L. A. *Chem. Mater.* **2008**, *20*, 6562–6566.
(34) Lou, X. W.; Li, C. M.; Archer, L. A. *Adv. Mater.* **2009**, *21*, 2536–2539.
(35) Lv, W.; Tang, D. M.; He, Y. B.; You, C. H.; Shi, Z. Q.; Chen, X. C.; Chen, C. M.; Hou, P. X.; Liu, C.; Yang, Q. H. *ACS Nano* **2009**, *3*, 3730–3736.
(36) Stankovich, S.; Dikin, D. A.; Dommett, G. H. B.; Kohlhaas, K. M.; Zimney, E. J.; Stach, E. A.; Piner, R. D.; Nguyen, S. T.; Ruoff, R. S. *Nature* **2006**, *442*, 282–286.
(37) Stoller, M. D.; Park, S. J.; Zhu, Y. W.; An, J. H.; Ruoff, R. S. *Nano Lett.* **2008**, *8*, 3498–3502.
(38) Stankovich, S.; Dikin, D. A.; Piner, R. D.; Kohlhaas, K. A.; Kleinhammes, A.; Jia, Y.; Wu, Y.; Nguyen, S. T.; Ruoff, R. S. *Carbon* **2007**, *45*, 1558–1565.
(39) Paek, S. M.; Yoo, E.; Honma, I. *Nano Lett.* **2009**, *9*, 72–75.
(40) Wang, D. H.; Choi, D. W.; Li, J.; Yang, Z. G.; Nie, Z. M.; Kou, R.; Hu, D. H.; Wang, C. M.; Saraf, L. V.; Zhang, J. G.; Aksay, I. A.; Liu, J. *ACS Nano* **2009**, *3*, 907–914.
(41) Yao, J.; Shen, X. P.; Wang, B.; Liu, H. K.; Wang, G. X. *Electrochem. Commun.* **2009**, *11*, 1849–1852.
(42) Wang, G. X.; Wang, B.; Wang, X. L.; Park, J.; Dou, S. X.; Ahn, H.; Kim, K. *J. Mater. Chem.* **2009**, *19*, 8378–8384.
(43) Wang, G. X.; Shen, X. P.; Yao, J.; Park, J. *Carbon* **2009**, *47*, 2049–2053.
(44) Yoo, E.; Kim, J.; Hosono, E.; Zhou, H.; Kudo, T.; Honma, I. *Nano Lett.* **2008**, *8*, 2277–2282.
(45) Chou, S. L.; Wang, J. Z.; Choucair, M.; Liu, H. K.; Stride, J. A.; Dou, S. X. *Electrochem. Commun.* **2010**, *12*, 303–306.
(46) Wu, Z. S.; Ren, W. C.; Wen, L.; Gao, L. B.; Zhao, J. P.; Chen, Z. P.; Zhou, G. M.; Li, F.; Cheng, H. M. *ACS Nano* **2010**, *4*, 3187–3194.
(47) Zhang, M.; Lei, D. N.; Yin, X. M.; Chen, L. B.; Li, Q. H.; Wang, Y. G.; Wang, T. H. *J. Mater. Chem.* **2010**, *20*, 5538–5543.

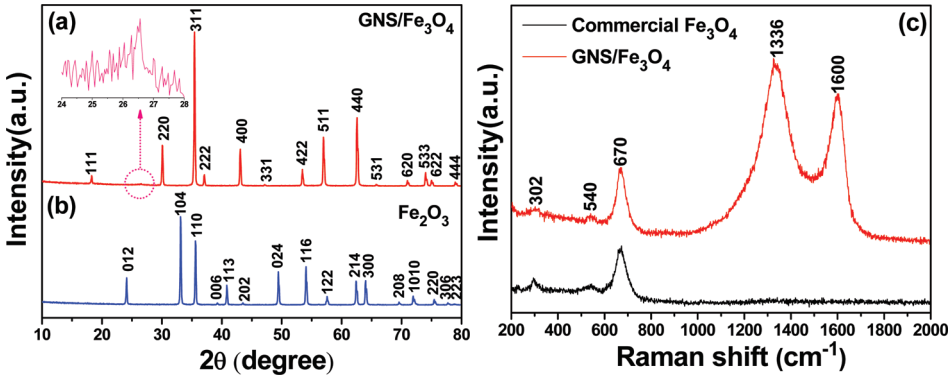

Figure 1. XRD profiles of (a) GNS/Fe_3O_4 composite and (b) bare Fe_2O_3 particles. (c) Raman spectra of the GNS/Fe_3O_4 composite and commercial Fe_3O_4 particles.

with Fe_3O_4 particles through in situ reduction of iron hydroxide between GNSs. It is found that the GNS/Fe_3O_4 composite has the advantages of the two building blocks and exhibits a large reversible capacity, enhanced cyclic stability, and excellent rate capability.

2. Experimental Section

Synthesis of the GNSs. GNSs were prepared from natural flake graphite powder by chemical exfoliation as reported elsewhere.[48] Three steps were involved in the graphene preparation: first, oxidation of the natural flake graphite powder to prepare graphite oxide using Hummers method;[49] second, fast thermal expansion/exfoliation of the graphite oxide (1050 °C, Ar, 30 s) to synthesize thermally expanded graphene oxide (TEGO); finally, hydrogen reduction of TEGO (400 °C, 2 h) to obtain GNSs.[50]

Synthesis of GNS/Fe_3O_4 Composite. Fifty milligrams of GNSs were dispersed in 150 mL of 0.05 mol/L $FeCl_3$ solution by sonication for 1 h, followed by hydrolysis of iron chloride hexahydrate ($FeCl_3 \cdot 6H_2O$) at 353 K for 12 h to obtain uniform spindle-shaped FeOOH particles embedded in GNSs, as shown in Figure S1 in the Supporting Information. The component was confirmed by X-ray diffraction (XRD) measurement (see Figure S2 in the Supporting Information) that showed all the diffraction peaks are consistent with the standard values for FeOOH (JCPDS No. 34−1266), which comes from the hydrolyzate of $FeCl_3 \cdot 6H_2O$. The resulting product was filtered and washed repeatedly with deionized water and dried under vacuum at 363 K for 24 h. Then the samples were heat-treated at 873 K with a heating rate of 5 °C min^{-1} and held for 4 h under argon atmosphere to reduce the spindle FeOOH to Fe_3O_4 in situ and form the GNS/Fe_3O_4 composite. According to thermogravimetric (TG) analyses (see Figure S3 in the Supporting Information), the weight percentage of graphene content is 13.3 wt % in the GNS/Fe_3O_4 composite.

Synthesis of Bare Fe_2O_3. The synthetic procedure is the same as that for GNS/Fe_3O_4 composite but without adding GNSs. The SEM image of the bare Fe_2O_3 particles is shown in Figure S4 in the Supporting Information.

Materials Characterization. The morphology and structure of the samples were characterized by a transmission electron microscope (TEM, Tecnai F20, 200 kV), scanning electron microscope (SEM, FEI Nova NanoSEM 430, 15 kV), micro-Raman spectroscope (Jobin Yvon LabRam HR800, excited by 632.8 nm He−Ne laser), and XRD (D-MAX/2400, Cu Kα). TG (Netzsch-STA 449C, measured from 30 to 1000 °C at a heating rate of 10 °C/min in air). N_2 adsorption/desorption isotherms were determined using Micromeritics ASAP 2010M.

Electrochemical Measurements. The electrochemical properties of the commercial Fe_3O_4 particles, GNS/Fe_3O_4 composite and bare Fe_2O_3 particles as anode materials in lithium ion cells were evaluated by galvanostatic charge/discharge technique. The test electrodes were prepared by mixing 80 wt % active material with 10 wt % conductive carbon black (super P) as a conductive agent and 10 wt % polyvinylidene fluoride (PVDF) dissolved in N-methyl-2-pyrrolidone (NMP) as a binder to form a slurry, which was then coated onto a copper foil, pressed and dried under vacuum at 120 °C for 12 h. Coin cells were finally assembled in an argon-filled glovebox with the commercial Fe_3O_4 particles, GNS/Fe_3O_4 composite or bare Fe_2O_3 particles as test electrode, metallic lithium as the counter/reference electrode, 1 M $LiPF_6$ in ethylene carbonate, diethyl carbonate and ethylmethyl carbonate (EC/DMC/EMC, 1:1:1 vol) electrolyte, and Celgard 2400 polypropylene as separator. Charge−discharge measurements were carried out galvanostatically at various current densities over a voltage range of 0.001−3 V (vs Li/Li^+) using a battery test system (LAND CT2001A model, Wuhan Jinnuo Electronics. Ltd.). After 30 cycles, the cells were disassembled in the glovebox, and the working electrode was taken out and washed three times using a DMC solution. It was then transferred using a sealed container into the vacuum chamber of the SEM for structure characterization.

3. Results and Discussion

Figure 1a shows the XRD profile of the GNS/Fe_3O_4 composite obtained after 873 K heat treatment through in situ reduction of iron hydroxide (see Figure S2 in the Supporting Information) by GNSs. All the peaks can be assigned to Fe_3O_4 (JCPDS No.65−3107). A diffraction hump appears in the range of 24−28°, which originates from GNSs (inset of Figure 1a). Figure 1b shows the XRD pattern of the product prepared using the same conditions but without adding GNSs. All the diffraction peaks are in good agreement with the standard profiles

(48) Wu, Z. S.; Ren, W. C.; Gao, L. B.; Liu, B. L.; Jiang, C. B.; Cheng, H. M. *Carbon* **2009**, *47*, 493–499.
(49) Hummers, W. S.; Offeman, R. E. *J. Am. Chem. Soc.* **1958**, *80*, 1339.
(50) Wang, D. W.; Li, F.; Zhao, J. P.; Ren, W. C.; Chen, Z. G.; Tan, J.; Wu, Z. S.; Gentle, I.; Lu, G. Q.; Cheng, H. M. *ACS Nano* **2009**, *3*, 1745–1752.

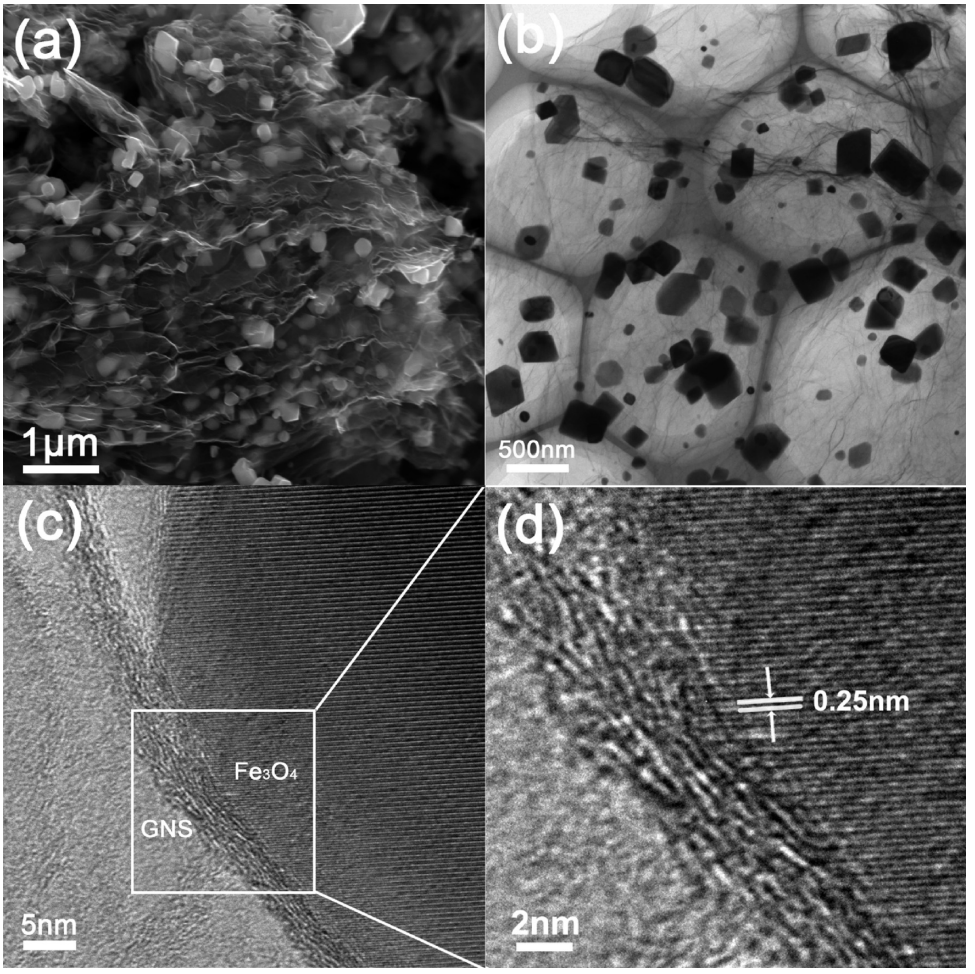

Figure 2. (a) SEM image of the cross-section of GNS/Fe_3O_4 composite, (b) TEM and (c) high-resolution TEM images of GNS/Fe_3O_4 composite, and (d) detailed interface structure of the square area in (c).

of Fe_2O_3 (JCPDS No. 33−0664). Raman spectra of the commercial Fe_3O_4 particles and GNS/Fe_3O_4 composite are shown in Figure 1c. The fundamental Raman scattering peaks for Fe_3O_4 powders are observed at 302, 540, and 670 cm^{-1} corresponding to the E_g, T_{2g}, and $A_{1\,g}$ vibration modes, respectively.[51,52] The Raman spectrum of the GNS/Fe_3O_4 composite shows typical peaks of magnetite and characteristic peaks of the D and G bands from GNS at around 1336 and 1600 cm^{-1}.[53]

The microstructure of the GNS/Fe_3O_4 composite was characterized by SEM and TEM. The SEM image taken from a typical cross-section of the GNS/Fe_3O_4 composite (Figure 2a) possesses a layer-by-layer assembled structure consisting of GNSs and Fe_3O_4 particles. The TEM image (Figure 2b) reveals that these Fe_3O_4 particles are firmly attached to the graphene sheets, even after the ultrasonication used to disperse the GNS/Fe_3O_4 composite for TEM characterization. As shown in Figure 2c, the Fe_3O_4 particle is wrapped by graphene sheets, which helps to prevent Fe_3O_4 from agglomeration and enables a good dispersion of these oxide particles over the graphene support. The high-resolution TEM image in Figure 2d shows the interfacial structure between GNS and the Fe_3O_4 particle. The well-resolved lattice fringes with an interplane distance of 0.25 nm come from the (311) plane of Fe_3O_4. The short-range disordered structure observed at the interfacial region of GNS and Fe_3O_4 may suggest formation of interfacial bonds for the stabilization of the oxide particles on the graphene support. Energy-dispersive X-ray spectroscopy elemental mapping was used to understand the distribution of Fe_3O_4 particles in the composite. From the elemental distribution of iron, oxygen, and carbon shown in Figure 3, we can recognize the uniform dispersion of the Fe_3O_4 particles in the stacked structure consisting of GNS/Fe_3O_4 hybrid sheets.

The porous structure characteristics and Brunauer−Emmett−Teller (BET) specific surface area of commercial Fe_3O_4 particles and the GNS/Fe_3O_4 composite were investigated by nitrogen isothermal adsorption (Figure 4). The BET specific surface area of GNS/Fe_3O_4 composite is 53 m^2/g, much higher than that of commercial Fe_3O_4 (2 m^2/g). The relatively large specific surface area is beneficial for electrolyte access. It can be seen from the SEM image (see Figure S5 in the Supporting Information) that the commercial Fe_3O_4 particles have an analogous morphology to the Fe_3O_4 particles in the GNS/Fe_3O_4

(51) deFaria, D. L. A.; Silva, S. V.; deOliveira, M. T. *J. Raman Spectrosc.* **1997**, *28*, 873–878.
(52) Shebanova, O. N.; Lazor, P. *J. Solid State Chem.* **2003**, *174*, 424–430.
(53) Ferrari, A. C.; Robertson, J. *Phys. Rev. B* **2000**, *61*, 14095–14107.

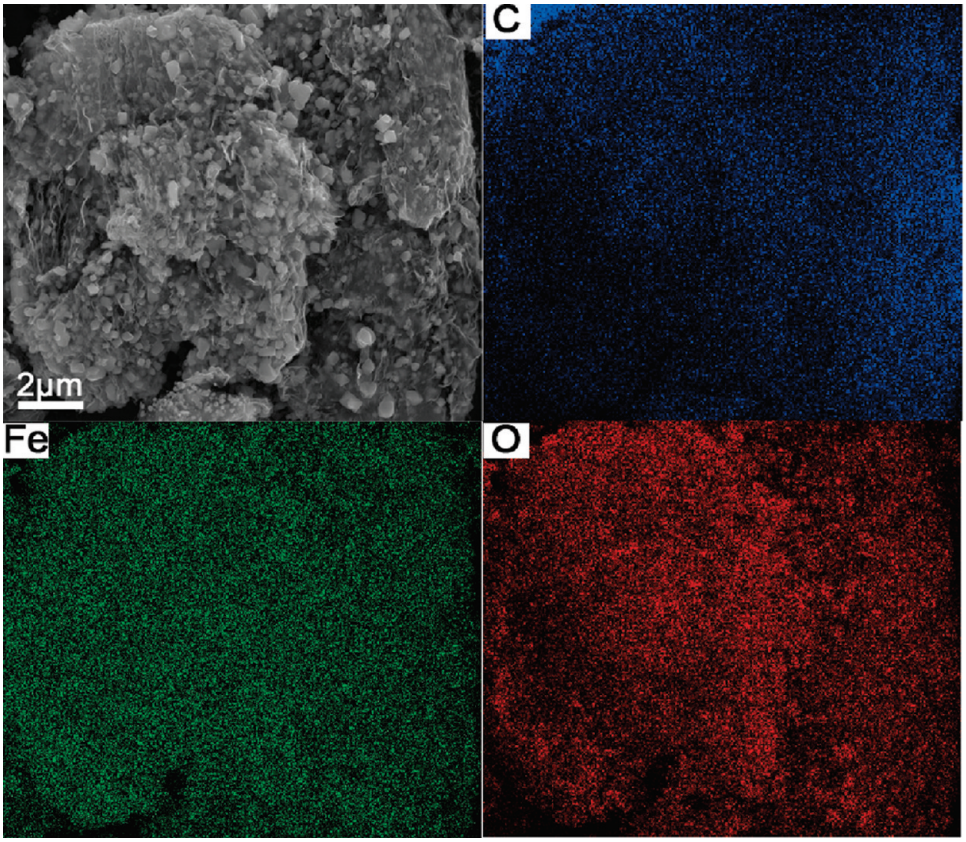

Figure 3. SEM image and corresponding carbon, iron, and oxygen elemental mapping of GNS/Fe_3O_4 composite.

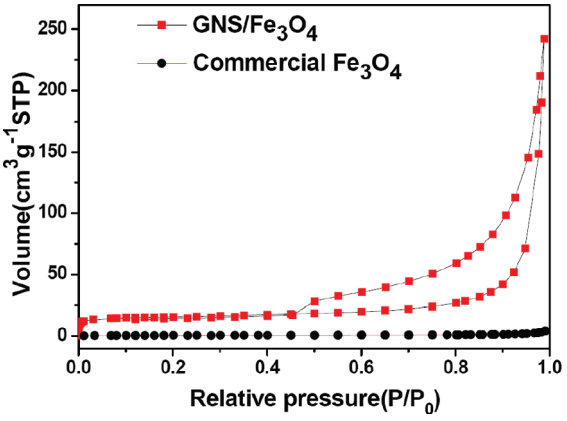

Figure 4. N_2 adsorption/desorption isotherms of commercial Fe_3O_4 particles and GNS/Fe_3O_4 composite.

composite, while negligible pore volume was observed. With respect to the GNS/Fe_3O_4 composite, the unique organization of the interlayered structure possesses a certain amount of macropores and mesopores that form an open porous system, and a limited amount of micropores and small mesopores with pore volume of 0.23 cm^3/g was confirmed by the nitrogen isothermal adsorption/desorption measurements. The porosity with a unique lateral wrapped structure containing a porous structure of macropores and mesopores may facilitate electrolyte ion diffusion to active sites with less resistance[54] and tolerate the volume change[55] of Fe_3O_4 particles during charge/discharge cycles, suggesting that the GNS/Fe_3O_4 composite may show large capacity, good rate performance and cycling stability.

To highlight the superiority of the unique GNS/Fe_3O_4 composite for anode materials of LIBs, we compared the electrochemical performance of the GNS/Fe_3O_4 composite, bare Fe_2O_3, and commercial Fe_3O_4 particles. Discharge/charge curves of the GNS/Fe_3O_4 composite (Figure 5a) were obtained at a current density of 35 mA g^{-1}. In the first discharge curve, an extended potential plateau at about 0.8 V versus Li^+/Li is observed for the GNS/Fe_3O_4 composite, similar to the literature results for Fe_3O_4.[17,19] The electrochemical reversible reaction can be summarized as

$$Fe_3O_4 + 8e^- + 8Li^+ \leftrightarrow 3Fe^0 + 4Li_2O$$

If 8 Li^+ were removed reversibly, a charge capacity of 922 mA h g^{-1} could be obtained.[18] In the first cycle, the charge capacity of the commercial Fe_3O_4 particles is ~770 mAh g^{-1}. However, it fades quickly (Figure 5b). On the contrary, the GNS/Fe_3O_4 composite has the first reversible capacity of 900 mA h g^{-1} and the capacity does not decrease through the subsequent discharge/charge cycles (Figure 5a). The irreversible capacity loss in the first cycle can be attributed to the formation of a

(54) Wang, D. W.; Li, F.; Liu, M.; Lu, G. Q.; Cheng, H. M. *Angew. Chem., Int. Ed.* **2008**, *47*, 373–376.

(55) Yang, S. B.; Cui, G. L.; Pang, S. P.; Cao, Q.; Kolb, U.; Feng, X. L.; Maier, J.; Mullen, K. *ChemSusChem*, **2010**, *3*, 236–239.

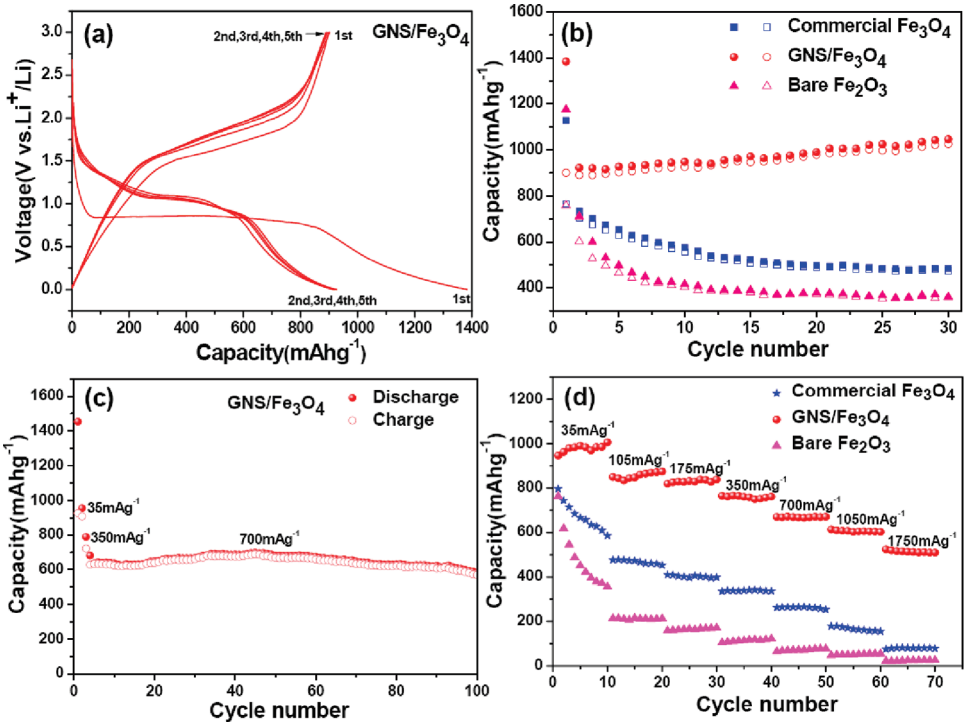

Figure 5. (a) Discharge/charge profiles of the GNS/Fe_3O_4 composite. (b) Cycling performance of the commercial Fe_3O_4 particles, GNS/Fe_3O_4 composite and bare Fe_2O_3 particles at a current density of 35 mA g^{-1}. Solid symbols, discharge; hollow symbols, charge. (c) Cycling performance of the GNS/Fe_3O_4 composite at a current density of 700 mA g^{-1} for 100 cycles. (d) Rate performance of the commercial Fe_3O_4 particles, GNS/Fe_3O_4 composite, and bare Fe_2O_3 particles at different current densities.

solid electrolyte interphase film, the decomposition of electrolyte and the reaction of oxygen-containing functional groups on graphene with lithium ions.[18,29,56,57] Besides, the inherent poor electrical/ionic conductivity of the Fe_3O_4/Fe/Li_2O matrix formed during the charge/discharge process may also cause irreversible lithium loss.[19,20,31] Figure 5b shows the discharge−charge cycling performance of the commercial Fe_3O_4 particles, GNS/Fe_3O_4 composite and bare Fe_2O_3 particles at a current density of 35 mA g^{-1} for 30 cycles. The capacities of the commercial Fe_3O_4 and bare Fe_2O_3 particles decrease from 770 and 760 mA h g^{-1} to 475 and 359 mA h g^{-1}, respectively. In a sharp contrast, the GNS/Fe_3O_4 composite electrode maintains a high reversibility, and its reversible capacity even gradually increases to 1026 mA h g^{-1}. The Coulombic efficiency of the GNS/Fe_3O_4 composite after the second cycle remains close to 100% until 30 cycles. Importantly, the GNS/Fe_3O_4 composite electrode, tested at a much higher current density of 700 mA g^{-1}, exhibits excellent cyclic performance, and retains 91% of its initial capacity after 100 cycles (Figure 5c). Moreover, another cell used for a long-term test that has been tested for about 7 months with 85 cycles at a current density of 35 mA g^{-1} is shown in Figure S6 in the Supporting Information, and it is still being tested. The charge capacity remains at 950 mA h g^{-1} after 85 cycles, indicating the enhanced cycling stability of the GNS/Fe_3O_4 composite. The above results can be ascribed to the flexible interleaved structure that favors fast electron and ion transport, as well as effectively limiting the volume expansion and detachment of Fe_3O_4 particles during cycling. It is interesting to note that the phenomenon of the gradual increased capacity, which is well-documented in the literature, is attributed to the reversible growth of a polymeric gel-like film resulting from kinetically activated electrolyte degradation.[58−60]

To further investigate the electrochemical performance of the commercial Fe_3O_4 particles, GNS/Fe_3O_4 composite and bare Fe_2O_3 particles, the rate capability of the samples is shown in Figure 5d. The GNS/Fe_3O_4 composite illustrates a much better rate performance, in particular, when the current density reaches 1750 mA g^{-1}, the specific capacity of the GNS/Fe_3O_4 composite still retains 520 mA h g^{-1}, 53% of the initial capacity. However, the capacities of the commercial Fe_3O_4 and bare Fe_2O_3 particles drop dramatically, only 10 and 3% of the initial capacity at this high charge rate. These results clearly show that the well-organized flexible interleaved structure plays an important role in improving the electrochemical performance. The high reversible capacity and improved cycle stability and rate performance can be attributed to the porosity between GNSs that is favorable for Li ion transport, the interleaved electron transfer highways built up from GNSs, and the flexible GNSs that play a "flexible confinement" function to enwrap

(56) Ban, C. M.; Wu, Z. C.; Gillaspie, D. T.; Chen, L.; Yan, Y. F.; Blackburn, J. L.; Dillon, A. C. *Adv. Mater.* **2010**, *22*, E145–E149.
(57) Guo, P.; Song, H. H.; Chen, X. H. *Electrochem. Commun.* **2009**, *11*, 1320–1324.
(58) Grugeon, S.; Laruelle, S.; Dupont, L.; Tarascon, J. M. *Solid State Sci.* **2003**, *5*, 895–904.
(59) Laruelle, S.; Grugeon, S.; Poizot, P.; Dolle, M.; Dupont, L.; Tarascon, J. M. *J. Electrochem. Soc.* **2002**, *149*, A627–A634.
(60) Do, J. S.; Weng, C. H. *J. Power Sources* **2005**, *146*, 482–486.

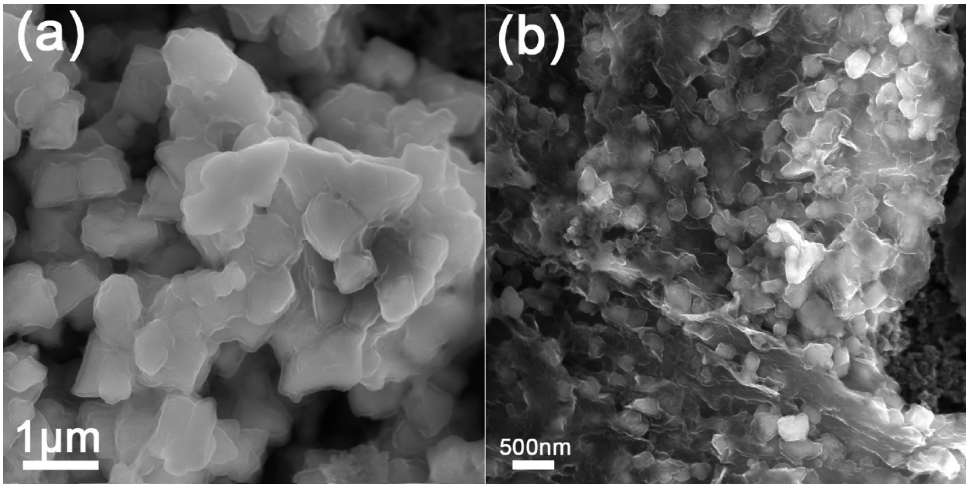

Figure 6. SEM images of (a) commercial Fe_3O_4 particles and (b) GNS/Fe_3O_4 composite after 30 discharge/charge cycles.

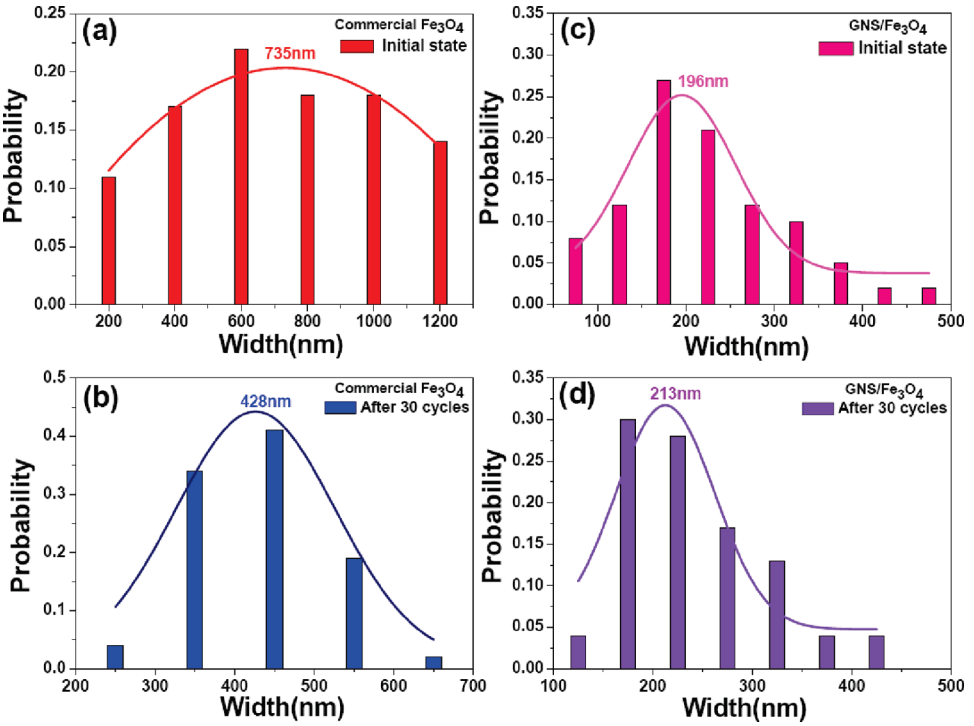

Figure 7. Size distributions of the commercial Fe_3O_4 particles (a) in initial state and (b) after 30 discharge/charge cycles, and the GNS/Fe_3O_4 composite (c) in initial state and (d) after 30 discharge/charge cycles.

Fe_3O_4 particles for inhibiting the volume change, alleviating the stress of Fe_3O_4 particles, and preventing the detachment and agglomeration of pulverized Fe_3O_4 during cycling.

To understand the excellent electrochemical performance of the unique layered composite, the morphology and microstructure variation of the commercial Fe_3O_4 particles and the GNS/Fe_3O_4 composite after 30 discharge/charge cycles were examined using SEM. It is obviously demonstrated that the Fe_3O_4 particles are isolated and well-dispersed in the initial state in Figure S5 in the Supporting Information. However, after 30 cycles, the particles become smaller and agglomerated (Figure 6a), with the average size decreasing from 735 to 428 nm (Figure 7a and b), indicating the pulverization of the particles during cycling that leads to the poor cycling stability of commercial Fe_3O_4 particles. In contrast, for the GNS/Fe_3O_4 composite, as shown in Figure 6b, the Fe_3O_4 particles are still closely embedded in graphene layers and the morphology as well as particle size are almost the same as in the initial state (Figure 7c, d). The fact that the Fe_3O_4 particles in the composite do not exhibit agglomeration or size variation indicates the important role of GNSs to flexibly enwrap Fe_3O_4 particles that can effectively accommodate the strain and stress of volume change and prevent the detachment and agglomeration of pulverized Fe_3O_4 during cycling, which consequently enhances the cyclic stability and rate capability.

4. Conclusion

We fabricated a flexible interleaved composite of GNSs and Fe_3O_4 particles as an anode material for LIBs. The GNSs in the flexible interleaved structure form an effective matrix for the individual dispersion of Fe_3O_4 particles, play a "flexible confinement" function for tolerating the volume change and preventing the detachment and agglomeration of pulverized Fe_3O_4 particles during cycling. They also act as an electron transport highway for improving the electrical conductivity, whereas the Fe_3O_4 particles inhibit the restacking of GNSs. The flexible interleaved structure contains some large-size porosity that can also facilitate fast ion transport. As a result, this flexible interleaved structure offers great advantages to enhance the lithium storage capacity, cyclic stability, and rate capability, indicating its promising potential for use as a novel anode material for high-performance LIBs for applications such as in electric vehicles.

Acknowledgment. This work was supported by National Science Foundation of China (Nos.50921004 and 50632040), K.C. Wong Education Foundation, Hong Kong, and Chinese Academy of Sciences (KGCX2-YW-231). We thank Mr. L. B. Gao, B. L. Liu, and S. F. Pei for helpful discussion,; Dr. D. M. Tang and Dr. C. B. Jiang for TEM support; and Prof. Peter Thrower for his constructive advice.

Supporting Information Available: Figures S1−S6 (PDF). This material is available free of charge via the Internet at http://pubs.acs.org.